Research Square

Preprints are preliminary reports that have not undergone peer review.
They should not be considered conclusive, used to inform clinical practice,
or referenced by the media as validated information.

Geometry-controlled vortex dynamics and critical currents in asymmetric superconducting loops with Dayem and nano-bridge weak links

C. A. Aguirre
caaguirret@udistrital.edu.co

Universidad Distrital Francisco José de Caldas

J. Faúndez
Universidad Andres Bello

D. Laroze
Universidad de Tarapacá

A. M. Vallejo
Universidad Nacional de Colombia

J. S. Victorino
Universidad Nacional de Colombia

J. Barba-Ortega
Universidad Nacional de Colombia

Research Article

Keywords: Mesoscopic superconductivity, vortex dynamics, weak links, Dayem-bridge, nano-bridge, time-dependent Ginzburg–Landau theory, critical current, phase slips

Posted Date: August 24th, 2026

DOI: https://doi.org/10.21203/rs.3.rs-10636928/v1

License: This work is licensed under a Creative Commons Attribution 4.0 International License.
Read Full License

Additional Declarations: No competing interests reported.

Geometry-controlled vortex dynamics and critical currents in asymmetric superconducting loops with Dayem and nano-bridge weak links.

C. A. Aguirre
Departamento de Física,
Universidad Distrital Francisco José de Caldas, Bogotá, Colombia.
Corresponding author: caaguirret@udistrital.edu.co.

J. Faúndez
Departamento de Física y Astronomía, Universidad Andres Bello, Santiago 837-0136, Chile.

D. Laroze
Instituto de Alta Investigación, Universidad de Tarapacá, Casilla 7D, Arica, Chile.

A. M. Vallejo, J. S. Victorino, and J. Barba-Ortega
Departamento de Física, Universidad Nacional de Colombia, Bogotá, Colombia.
(Dated: August 11, 2026)

We study vortex patterns and transport behavior in an asymmetric mesoscopic superconducting loop that incorporates two non-equivalent constriction-type weak links: a Dayem-bridge and a nano-bridge. Employing time-dependent Ginzburg–Landau simulations in the thin-film limit, we examine the magnetization, spatial distribution of supercurrents, Cooper-pair density, voltage response, and current–phase characteristics in the presence of perpendicular magnetic fields and applied transport currents. Without transport current, the geometric asymmetry generates non-uniform vortex arrangements and alters the local circulation of supercurrents. When a current bias is applied, the two constrictions display different degrees of order-parameter suppression, giving rise to distinct voltage responses and critical-current values. By tuning the bridge widths, we demonstrate that both the onset of the resistive state and the resulting vortex configuration can be tailored geometrically. Collectively, our findings identify asymmetric mesoscopic loops as an adjustable platform for engineering vortex entry, phase-slip processes, and critical currents in superconducting circuits based on weak links.

Key Words: Mesoscopic superconductivity; vortex dynamics; weak links; Dayem-bridge; nano-bridge; time-dependent Ginzburg–Landau theory; critical current; phase slips.

I. INTRODUCTION

Mesoscopic superconducting structures provide a versatile platform in which geometrical design can be harnessed to control vortex matter, phase-slip dynamics, and critical-current thresholds. As the dimensions of a superconducting film or loop approach the characteristic superconducting length scales, the nucleation, motion, and stability of vortices are strongly affected by spatial confinement, sample boundaries, surface barriers, defects, overall topology, and local changes in the superconducting cross-sectional area [1–5]. As a result, even small geometric adjustments can significantly modify the magnetization, current distribution, vortex configurations, and the corresponding voltage responses. This strong dependence on geometry makes mesoscopic superconductors attractive candidates for use in superconducting electronics, flux-based sensors, and superconducting quantum interference devices [6–12].

An important strategy for engineering these responses is to use weak links. In contrast to tunnel Josephson junctions, constriction-type weak links—such as Dayem-bridges and nano-bridges—are fabricated directly from the superconducting film. Their transport properties are governed not only by the phase difference across the constriction, but also by order-parameter suppression, current crowding, vortex entry, and phase-slip processes [13–15]. As a result, their critical current depends strongly on the bridge width and length, as well as on how the bridge is connected to the superconducting banks. In asymmetric mesoscopic loops, dissimilar weak links can break reflection symmetry, leading to different local barriers for vortex penetration and distinct resistive characteristics. In addition, the interplay between geometry, vortex dynamics, and transport is fundamental in type-II superconductors, where magnetic flux penetrates the material in the form of quantized vortices. Under an applied magnetic field, vortices nucleate at the sample boundaries and arrange themselves according to confinement, surface barriers, vortex–vortex interactions, and the specific features of the superconducting geometry [16–20]. When a transport current flows, vortex motion and phase-slip events can drive the system into a finite-voltage state once the critical current is surpassed [14, 15, 18]. Therefore, understanding how weak-link geometry influences these processes is essential for designing superconducting devices with tunable response characteristics.

The time-dependent Ginzburg–Landau (**TDGL**) theory offers a suitable phenomenological framework for exploring these effects in mesoscopic superconductors. In this

formalism, the superconducting order parameter, as well as the scalar and vector potentials and the current density, are obtained in a self-consistent manner, enabling the analysis of both magnetic-field-induced vortex patterns and current-driven resistive states [14, 17, 21]. Simulations based on the **TDGL** equations have been widely used to describe vortex penetration, current-driven suppression of superconductivity, phase-slip dynamics, voltage formation, and geometry-dependent transport in confined superconducting films and weak-link structures [14–17, 21]. Asymmetric superconducting structures are likewise significant in the wider field of nonreciprocal superconducting transport, where broken spatial symmetries, vortex motion, and current-driven suppression of superconductivity can lead to direction-dependent critical currents and voltage characteristics [22–33]. In this work, the goal is not to demonstrate a superconducting diode effect, but instead to determine how geometric asymmetry alters vortex penetration, phase-slip behavior, and critical-current thresholds.

In this study, we analyze an asymmetric mesoscopic superconducting loop that incorporates two distinct constriction-based weak links: a Dayem-bridge and a nano-bridge. Using the time-dependent Ginzburg–Landau equations in the thin-film limit, we demonstrate that geometric asymmetry has a pronounced impact on vortex nucleation, suppression of the order parameter, voltage characteristics, current–phase relationships, and critical-current thresholds. Our findings indicate that asymmetric weak-link designs provide a direct means to control vortex dynamics, phase-slip events, and superconducting transport in mesoscopic circuits.

This paper is organized as follows. In Sec. II, we introduce the theoretical model and numerical method. In Sec. III, we present the numerical results. Finally, Sec. IV summarizes the main conclusions.

II. MODEL AND METHODOLOGY

We study an asymmetric mesoscopic superconducting loop containing two non-equivalent constriction-type weak links: a Dayem-bridge and a nano-bridge, as illustrated in Fig. 1. A magnetic field $\mathbf{H} = H_z\hat{z}$ is applied perpendicular to the superconducting film, and a transport current is injected and collected through lateral contacts. The system is modeled using the generalized time-dependent Ginzburg–Landau formalism in the thin-film limit [14, 17, 21]. Unless otherwise stated, all physical quantities are expressed in dimensionless **TDGL** units. The superconducting order parameter $\psi(\mathbf{r},t)$ evolves according to the generalized Kramer–Watts–Tobin form of the **TDGL** equation [14, 17, 21],

$$\frac{\partial_t\psi + \psi\left(\frac{\Gamma^2}{2}\partial_t|\psi|^2 + i\Phi\right)}{\sqrt{1+\Gamma^2|\psi|^2}} = (i\nabla+\mathbf{A})^2\psi + \psi(1-|\psi|^2). \quad (1)$$

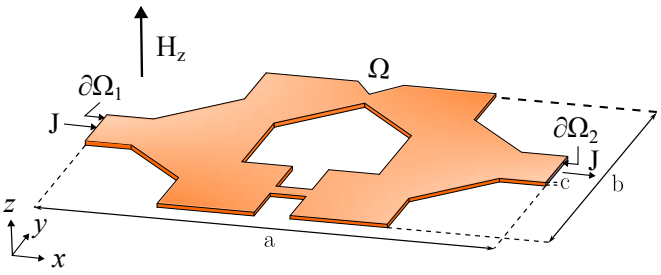


FIG. 1. Schematic representation of the asymmetric mesoscopic superconducting loop. The device contains two inequivalent constriction-based weak links, a Dayem-bridge and a nano-bridge, located on opposite sides of the loop. The magnetic field $\mathbf{H} = H_z\hat{z}$ is applied perpendicular to the film, and the transport current $\mathbf{J}$ is injected and extracted through the lateral contacts $\partial\Omega_i$, with $i = 1,2$. The geometrical dimensions are $a = 20\,\mu$m, $b = 10\,\mu$m, and $c = 0.1\,\mu$m.

Here, $\mathbf{A}$ is the vector potential, Φ is the scalar potential, and Γ controls the relaxation of the order-parameter amplitude. The total current density is written as

$$\mathbf{J} = \mathrm{Re}\,[\bar{\psi}(-i\nabla - \mathbf{A})\psi] - \nabla\Phi, \quad (2)$$

where the first term corresponds to the superconducting contribution and the second term represents the normal contribution [14, 17, 21]. Charge conservation leads to the Poisson equation for the scalar potential,

$$\nabla^2\Phi = -\nabla\cdot\mathbf{J}. \quad (3)$$

Current injection and extraction are implemented through Neumann boundary conditions at the lateral contacts, $\hat{\mathbf{n}}\cdot\nabla\Phi = \pm J$, where the plus and minus signs correspond to the two opposite electrodes. On all remaining boundaries, we impose $\hat{\mathbf{n}}\cdot\nabla\Phi = 0$. Since a purely Neumann boundary-value problem determines the scalar potential only up to an arbitrary additive constant, the voltage reference is fixed by setting the mean scalar potential on one electrode to zero [14, 21]. The instantaneous voltage is then computed as

$$V(t) = \langle\Phi\rangle_{\partial\Omega_1} - \langle\Phi\rangle_{\partial\Omega_2}, \qquad \langle\Phi\rangle_S = \frac{1}{|S|}\int_S \Phi\, dS, \quad (4)$$

where S denotes the corresponding contact surface. The voltage reported in the numerical results is obtained by time averaging $V(t)$ after the system has reached a stationary dynamical regime. For the superconducting order parameter, we impose the de Gennes boundary condition [4, 14, 21],

$$\hat{\mathbf{n}}\cdot(-i\nabla - \mathbf{A})\psi = \frac{i}{b}\psi, \quad (5)$$

where b is the de Gennes extrapolation length. In the present simulations, we take $b \to \infty$ at the superconductor–vacuum interfaces, enforcing a vanishing normal supercurrent across the boundary. This choice is appropriate when surface pair-breaking effects are not explicitly included.

The Ginzburg–Landau parameter is defined as $\kappa = \lambda/\xi$, where λ is the magnetic penetration depth and ξ is the superconducting coherence length. We set $\kappa = 2.0$, corresponding to a type-II superconducting regime. Spatial coordinates are measured in units of ξ, the order parameter is normalized by ψ_∞, the magnetic field by H_{c2}, and the vector potential by ξH_{c2}. Time is measured in units of the Ginzburg–Landau relaxation time. The numerical parameters are chosen as $\delta x = \delta y = \delta z = 0.1$, $\eta = 5.79$, $\beta = 1.0$, $\zeta = 0.50$, $\nu = 0.03$, and $\Gamma = 10$ [21]. The convergence tolerance for the order parameter is fixed at $\varepsilon = 10^{-9}$. The **TDGL** equations are solved self-consistently using a finite-volume discretization on an unstructured Delaunay triangulation, which is particularly suitable for narrow constrictions and asymmetric mesoscopic geometries [21]. The discrete **TDGL** equation for the order parameter at vertex i is:

$$\frac{u(\psi_i^{n+1}e^{i\mu_i^n\Delta t^n}-\psi_i^n)}{\Delta t^n\sqrt{1+\gamma^2|\psi_i^n|^2}}+\frac{u\gamma^2\left(|\psi_i^{n+1}|^2-|\psi_i^n|^2\right)\psi_i^n}{2\Delta t^n\sqrt{1+\gamma^2|\psi_i^n|^2}} = \left(\varepsilon_i-|\psi_i^n|^2\right)\psi_i^n+\frac{1}{a_i}\sum_{j\in\mathcal{N}(i)}\frac{U_{ij}^n\psi_j^n-\psi_i^n}{e_{ij}}s_{ij}. \tag{6}$$

Here, $\mathcal{N}(i)$ denotes the set of neighboring vertices, a_i is the area of the corresponding Voronoi cell, e_{ij} is the distance between neighboring vertices, s_{ij} is the length of the common Voronoi edge, and U_{ij}^n is the gauge-link variable. The scalar potential is obtained from the discrete current-conservation equation [21],

$$\sum_{j\in\mathcal{N}(i)}\frac{\mu_j^n-\mu_i^n}{e_{ij}}s_{ij} = \sum_{j\in\mathcal{N}(i)}\mathrm{Im}\left[(\psi_i^n)^*\frac{U_{ij}^n\psi_j^n-\psi_i^n}{e_{ij}}\right]|s_{ij}| - \sum_{j\in\mathcal{N}(i)}\frac{A_{ij}^n-A_{ij}^{n-1}}{\Delta t^n}|s_{ij}|. \tag{7}$$

The time step satisfies the stability condition $\Delta t \le \min\{dt_1, dt_2, dt_3\}$ [21], with $dt_1 = \frac{a\eta}{4\sqrt{1+\Gamma^2}}$, $dt_2 = \frac{a\beta}{4\kappa^2}$, $dt_3 = \frac{a\nu}{4\zeta^2}$, and:

$$a^2 = \frac{2}{\frac{1}{\delta x^2}+\frac{1}{\delta y^2}+\frac{1}{\delta z^2}}. \tag{8}$$

The numerical sample has dimensions $A = 30\xi$, $B = 15\xi$, and $C = 0.1\xi$. Both the Dayem-bridge and the nano-bridge are modeled as constriction-type weak links made of the same superconducting material, rather than being treated as ideal tunnel Josephson junctions. Therefore, their current–phase characteristics are obtained directly from the **TDGL** solution. This approach is more appropriate for constriction-based weak links, where the current–phase relation can deviate from the ideal sinusoidal Josephson form because of order-parameter suppression, current crowding, vortex penetration, and phase-slip dynamics [13–15]. For each bridge, the gauge-invariant phase difference is evaluated as

$$\Theta = \phi_B - \phi_A - \int_A^B \mathbf{A}\cdot d\mathbf{l}, \tag{9}$$

where A and B denote points located on opposite sides of the corresponding weak link. The local current through each bridge is calculated from Eq. (2), allowing the current–phase relation to be extracted without imposing an ideal sinusoidal dependence. This is essential because constriction-type weak links can display non-sinusoidal behavior associated with order-parameter suppression, current redistribution, and vortex-driven phase slips [13–15]. In the following sections, this model is used to analyze magnetic-field-induced vortex states, current-driven finite-voltage regimes, and geometry-dependent critical-current thresholds obtained by systematically varying the widths of the Dayem-bridge and the nano-bridge.

III. NUMERICAL RESULTS

In this section, we report the numerical results for the asymmetric mesoscopic superconducting loop shown in Fig. 1. The discussion is divided into three parts. First, we examine the vortex states induced by the magnetic field in the absence of any transport current. Second, we explore the current-driven finite-voltage response at zero magnetic field and compare the local behavior of the Dayem-bridge with that of the nano-bridge. Third, we analyze how changes in the width of each weak link affect the critical-current threshold and the corresponding vortex configurations.

A. Magnetic-field-induced vortex states

We begin by examining the magnetic response of the superconducting loop in the absence of transport current, $\mathbf{J} = 0$. With the simulations carried out at $\kappa = 2.0$, the system is firmly within the type-II superconducting regime. Figure 2 presents the magnetization as a function of the applied magnetic field, which is swept from 0 to 3.5 mT. At low fields, the magnetization exhibits the characteristic diamagnetic behavior of the Meissner–Ochsenfeld phase. As the field is raised, abrupt steps emerge in the magnetization curve. These discontinuities correspond to the entry of individual flux quanta into the mesoscopic loop. At sufficiently high fields, the gradual weakening of the superconducting signal signals the crossover toward the normal state.

These step-like features in the magnetization underscore the mesoscopic nature of the system, in which vortices enter via discrete, field-driven transitions rather than a smooth evolution. The observed vortex patterns arise from the interplay between vortex–vortex interactions, surface barriers, geometric confinement, and the nonuniform current distribution enforced by the asymmetric weak-link geometry.

To illustrate the vortex state induced by the magnetic field, Fig. 3 displays the supercurrent streamlines at $\mathbf{H} = 0.7$ mT and $\mathbf{J} = 0$. The current pattern is clearly influenced by the asymmetric shape of the loop and by the presence of two inequivalent weak links. As a result, the streamlines are

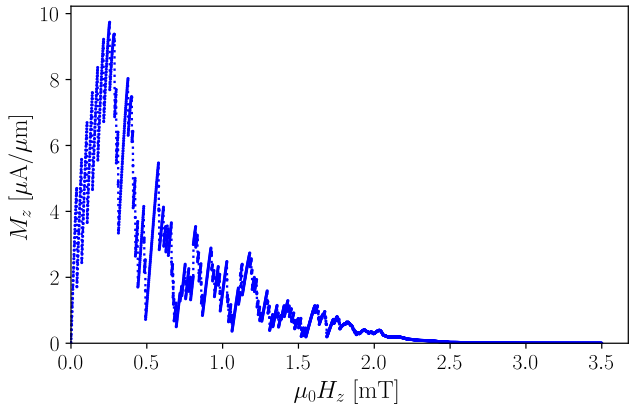


FIG. 2. Magnetization **M** of the asymmetric superconducting loop as a function of the applied magnetic field **H**, for zero transport current, $\mathbf{J} = 0$. The magnetic field is varied from 0 to 3.5 mT. The discontinuities in the magnetization curve indicate successive vortex-entry events in the mesoscopic superconducting loop.

not symmetric with respect to the sample's reflection axes. The supercurrent preferentially flows along the sample edges and encircles the regions where vortices are stabilized. The opposite sense of circulation on different sides of the loop is consistent with the emergence of localized vortex structures within the superconducting region. The corresponding

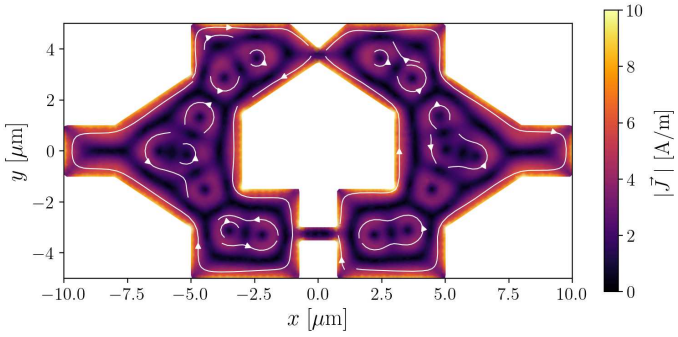


FIG. 3. Supercurrent streamlines in the asymmetric superconducting loop for an applied magnetic field $\mathbf{H} = 0.7$ mT and zero transport current, $\mathbf{J} = 0$. The asymmetric weak-link geometry produces an inhomogeneous current distribution and favors non-equivalent vortex-stabilization regions inside the loop.

Cooper-pair density, $|\psi|^2$, is displayed in Fig. 4. Vortices manifest as localized reductions in the magnitude of the order parameter and are situated close to the centers of the circulating supercurrent patterns depicted in Fig. 3. The vortex configuration is asymmetric, reflecting the spatial symmetry breaking induced by the Dayem-bridge and the nano-bridge. At the illustrated field value, the vortices remain distant from the weak-link constrictions, showing that the bridge geometry alters the current distribution without necessarily driving vortex nucleation within the constricted regions.

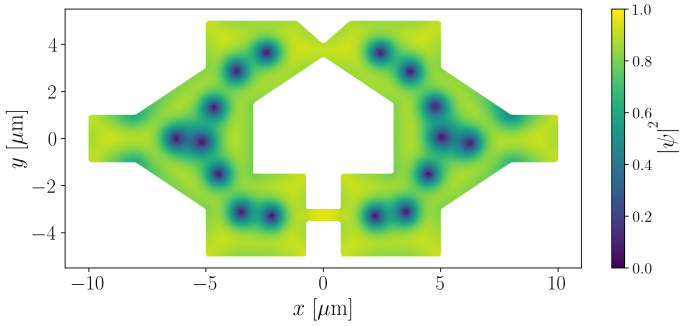


FIG. 4. Cooper-pair density $|\psi|^2$ for $\mathbf{H} = 0.7$ mT and $\mathbf{J} = 0$, after the system reaches a stable vortex configuration. The vortices are identified by local suppressions of the order parameter and are located near the centers of the supercurrent circulations.

The results shown in Figs. 2–4 characterize how the asymmetric loop responds to a magnetic field when no transport current is applied. They demonstrate that the weak-link geometry modifies the spatial pattern of screening currents and leads to asymmetric vortex arrangements, thereby laying the groundwork for the analysis of the current-driven response in the next subsection.

B. Current-driven finite-voltage response and weak-link phase dynamics

We now examine how the superconducting loop responds to an applied transport current when no external magnetic field is present. Figure 5 displays the voltage as a function of the applied current. Three voltage traces are shown: the spatially averaged response of the entire superconducting film, the local voltage across the Dayem-bridge, and the local voltage across the nano-bridge. At low currents, the voltage remains essentially zero, consistent with a superconducting state without sustained dissipative behavior. Once the current exceeds a critical threshold, a finite voltage emerges, signaling the onset of a current-driven resistive state. The two weak links produce distinct local voltage characteristics. This contrast arises from the different current-crowding patterns and degrees of order-parameter suppression in the Dayem-bridge and the nano-bridge. In the finite-voltage regime, the slopes of the voltage–current curves reflect different differential resistances for the two constrictions. Because no external ac drive is applied, these voltage onsets should be understood as current-induced transitions to a finite-voltage state—linked to phase-slip and vortex-mediated dynamics—rather than as Shapiro steps.

The spatial profile of the current-driven state is displayed in Fig. 6, where the Cooper-pair density is shown for $\mathbf{J} = 10\ \mu$A and $\mathbf{H} = 0$. The order parameter is markedly reduced in the vicinity of the weak links and near the regions where the current is injected. These localized reductions signal the emergence of areas in which superconductivity is diminished

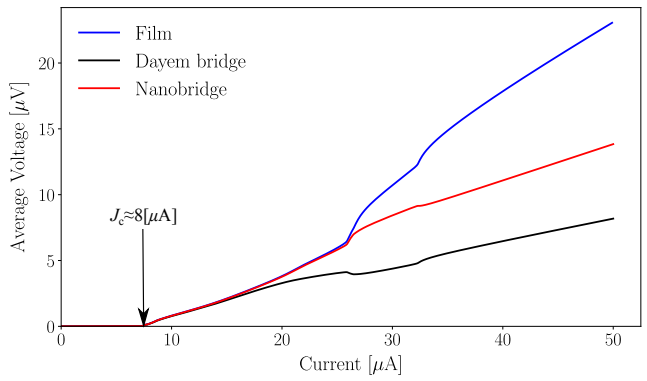


FIG. 5. Voltage response as a function of the applied transport current for zero external magnetic field, $\mathbf{H} = 0$. The curves correspond to three different measurements: the average response of the superconducting film, the local voltage across the Dayem-bridge, and the local voltage across the nano-bridge. The onset of a finite voltage defines a current-driven resistive threshold.

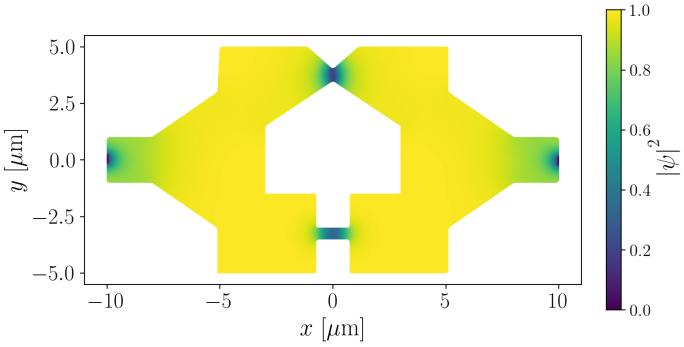


FIG. 6. Cooper-pair density $|\psi|^2$ in the asymmetric superconducting loop for zero applied magnetic field, $\mathbf{H} = 0$, and transport current $\mathbf{J} = 10\ \mu$A. The order parameter is locally suppressed near the weak links and current-injection regions, indicating the onset of current-driven dissipative dynamics.

by the applied current. The remainder of the sample stays largely superconducting, indicating that the transition to the finite-voltage state is spatially nonuniform and is governed by the constricted weak-link regions.

Figures 7 and 8 present the current–phase relations obtained from the **TDGL** solution for the nano-bridge and the Dayem-bridge, respectively. The two curves are clearly distinct, demonstrating that the constrictions function as different types of weak links. Both the maximum current and the phase at which it is reached vary between the two bridges, indicating differing degrees of local suppression of the superconducting order parameter and distinct current distributions imposed by the asymmetric geometry. Here, the current–phase relation is not imposed to be sinusoidal. Rather, it is computed directly from the local **TDGL** current and the gauge-invariant phase drop across each weak link. This is crucial, because constriction-based weak links can depart from the ideal Josephson behavior due to order-parameter depletion, current crowding, and vortex-mediated phase slips. Consequently, juxtaposing Figs. 7 and 8 yields a direct assessment of how the two weak links make different contributions to the phase dynamics of the loop.

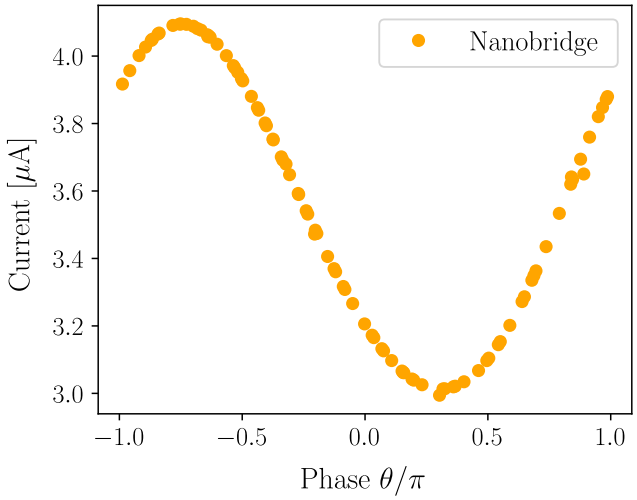


FIG. 7. Current–phase relation extracted from the **TDGL** solution for the nano-bridge. The curve reflects the local current response of the constriction as a function of the gauge-invariant phase difference across the weak link.

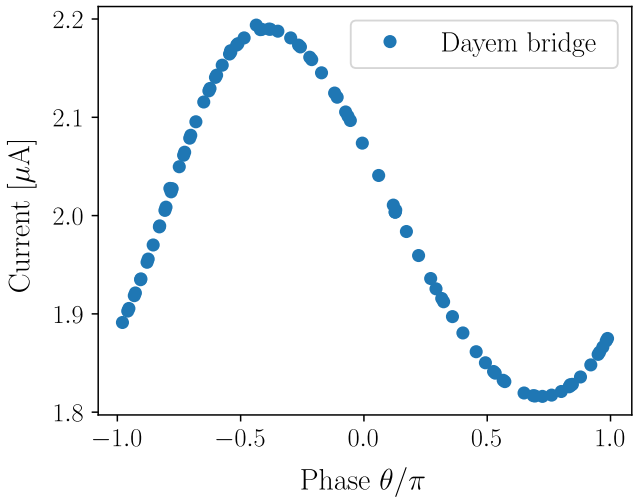


FIG. 8. Current–phase relation extracted from the **TDGL** solution for the Dayem-bridge. Comparison with Fig. 7 shows that the two constrictions have different phase-dependent current responses.

A more direct comparison between the two weak links is shown in Fig. 9, where the order-parameter density is projected along the bridge sections. Under identical applied-current conditions, the nano-bridge maintains a higher value of $|\psi|^2$ than the Dayem-bridge. This demonstrates that the superconducting condensate experiences stronger suppression in the Dayem-bridge, whereas the nano-bridge stays closer to

the fully superconducting regime. The resulting difference in the spatial profile of the order parameter accounts for the distinct voltage responses and current–phase relations reported in Figs. 5–8. Consequently, the two constrictions function as inequivalent weak links, with their transport properties governed by their respective geometries.

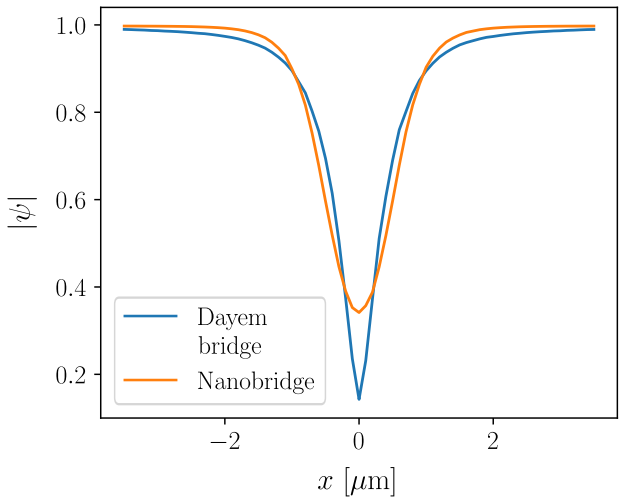


FIG. 9. Comparison of the projected Cooper-pair density $|\psi|^2$ along the Dayem-bridge and the nano-bridge for the same applied-current condition and zero external magnetic field. The different local suppression of $|\psi|^2$ demonstrates that the two constrictions behave as inequivalent weak links.

C. Geometry-controlled critical-current thresholds and vortex configurations

We now analyze how the weak-link geometry influences both the finite-voltage characteristics and the corresponding vortex configurations. To this end, we vary the width of one bridge while keeping the other fixed, and compute the voltage as a function of the applied transport current. The external magnetic field is set to $\mathbf{H} = 10$ mT. This configuration allows us to separate the individual contributions of the Dayem-bridge and the nano-bridge to the current-driven transition. The field value $\mathbf{H} = 10$ mT is chosen so that the system is well within the mixed-state regime, where vortex structures are sufficiently developed to make the effects of the weak-link geometry clearly visible. For each geometry, the critical current is determined using a small-voltage criterion, defined as the current at which the time-averaged voltage rises above the numerical noise floor. Figure 10 presents the voltage response for several Dayem-bridge widths, with the nano-bridge width held fixed. As the Dayem-bridge becomes wider, the onset of the finite-voltage state moves to higher applied currents. This trend shows that a wider Dayem-bridge can sustain larger supercurrents before the order parameter is sufficiently suppressed to initiate dissipative dynamics. In contrast, narrower bridges lower the critical current and promote an earlier transition into the resistive regime. Within the finite-voltage range, the variation of the slopes indicates that the effective differential resistance is likewise influenced by the bridge width.

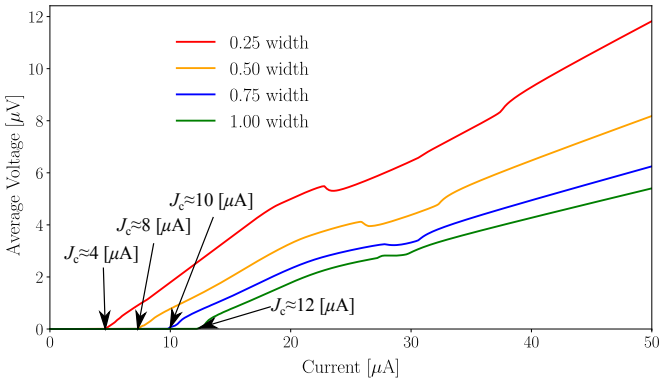


FIG. 10. Voltage response as a function of the applied current for different widths of the Dayem-bridge. The external magnetic field is fixed at $\mathbf{H} = 10$ mT, while the nano-bridge width is kept constant. Wider Dayem-bridges increase the current threshold for the onset of the finite-voltage state.

Figure 11 presents the analogous analysis for various nano-bridge widths, with the Dayem-bridge kept constant. The nano-bridge width also governs the onset of the finite-voltage state: narrower nano-bridges exhibit lower critical currents, whereas wider nano-bridges can carry higher currents before switching to the resistive regime. In contrast to tuning the Dayem-bridge, adjusting the nano-bridge width leads to a more substantial alteration of the voltage response, demonstrating that this constriction has a strong influence on the current-driven stability of the superconducting loop.

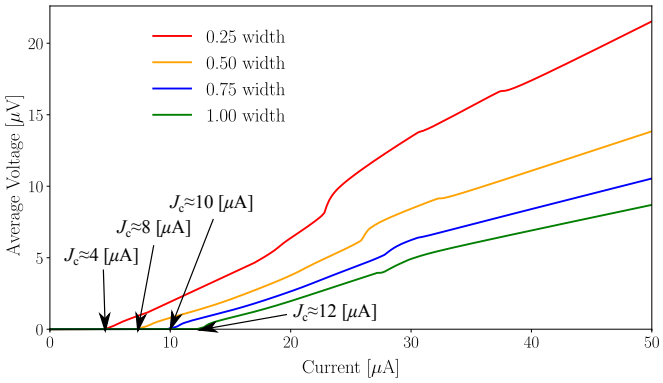


FIG. 11. Voltage response as a function of the applied current for different widths of the nano-bridge. The external magnetic field is fixed at $\mathbf{H} = 10$ mT, while the Dayem-bridge width is kept constant. The nano-bridge width strongly affects the current threshold and the finite-voltage response.

The effect of the nano-bridge width on the vortex configuration is presented in Fig. 12. The Cooper-pair density is shown for two different nano-bridge widths, while the Dayem-bridge is kept unchanged, under identical applied field

and current conditions. The two panels exhibit distinct vortex patterns, indicating that the weak-link geometry influences not only the voltage response but also the spatial distribution of the superconducting condensate. For the larger nano-bridge width, vortices are more strongly localized near the central part of the loop, pointing to enhanced vortex clustering driven by altered current flow and confinement barriers.

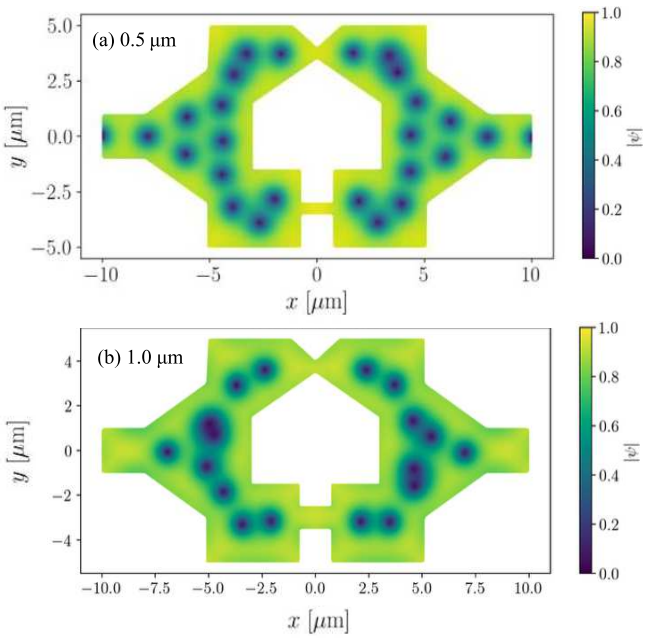


FIG. 12. Cooper-pair density $|\psi|^2$ for two different nano-bridge widths: (a) 0.5 μm and (b) 1.0 μm. The Dayem-bridge width is kept fixed. Both panels correspond to the same external magnetic field, $\mathbf{H} = 10$ mT, and transport current, $\mathbf{J} = 10\,\mu$A. The nano-bridge width modifies the vortex arrangement inside the loop.

Finally, Fig. 13 presents the Cooper-pair density for two distinct Dayem-bridge widths, while the nano-bridge width is held constant. The vortex pattern is once more reshaped by the modification of the weak-link geometry. Specifically, widening the Dayem-bridge changes the current distribution around the constriction and shifts the regions in which vortices are stabilized. These findings demonstrate that both weak links contribute to determining the mixed-state configuration, although their respective impacts on the voltage response and vortex arrangement are not the same.

Overall, the findings show that the asymmetric loop geometry offers a direct means of regulating vortex entry, current-induced finite-voltage transitions, and the local phase behavior of the weak links. The Dayem-bridge and the nano-bridge exhibit different responses to magnetic field and transport current, which results in distinct patterns of order-parameter suppression, voltage signatures, and current–phase relations. By adjusting the bridge widths, one can geometrically tune both the critical-current threshold and the vortex configuration, which constitutes the main outcome of this study.

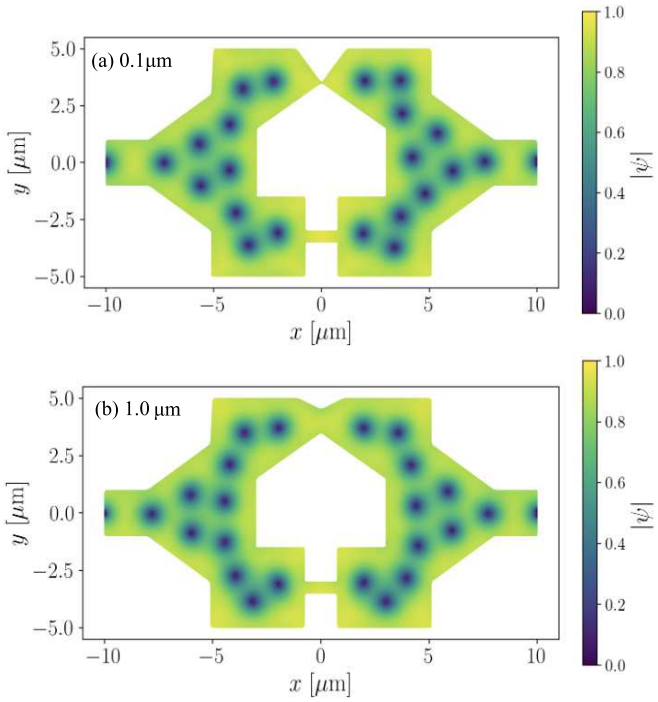


FIG. 13. Cooper-pair density $|\psi|^2$ for two different Dayem-bridge widths: (a) 0.1 μm and (b) 1.0 μm. The nano-bridge width is kept fixed. Both panels correspond to $\mathbf{H} = 10$ mT and $\mathbf{J} = 10\,\mu$A. The Dayem-bridge width modifies the vortex distribution and the local suppression of the superconducting order parameter.

IV. CONCLUSIONS

We studied the vortex configurations, the current-driven finite-voltage behavior, and the weak-link phase dynamics in an asymmetric mesoscopic superconducting loop that incorporates two non-equivalent constriction-type weak links: a Dayem-bridge and a nano-bridge. The system was described using the generalized time-dependent Ginzburg–Landau formalism in the thin-film approximation, which enabled a self-consistent calculation of the superconducting order parameter, supercurrent distribution, scalar potential, and the local current–phase characteristics. When no transport current is applied, the magnetization curve exhibits the typical behavior of a mesoscopic type-II superconducting loop, featuring discrete jumps linked to vortex-entry events. The associated supercurrent streamlines and Cooper-pair density distributions reveal that the asymmetric geometry creates distinct, non-equivalent regions where vortices can be stabilized. Specifically, the Dayem-bridge and the nano-bridge perturb the current flow in different ways, resulting in asymmetric vortex configurations even under a spatially uniform applied magnetic field. When a transport current is driven through the system at zero magnetic field, a finite voltage appears once the current exceeds a critical threshold. Spatially resolved voltage measurements show that the two weak links do not play equivalent roles in establishing this current-induced resistive state. The Dayem-bridge and the

nano-bridge display different degrees of order-parameter suppression, distinct differential voltage responses, and unequal current–phase relations. These disparities stem from the constriction-based character of the weak links, where current crowding, local depletion of the superconducting condensate, and vortex-mediated phase slips alter the transport behavior beyond the ideal sinusoidal Josephson regime.

We further showed that both the critical-current threshold and the vortex arrangement can be adjusted by varying the widths of the Dayem-bridge and the nano-bridge. Wider bridges support higher supercurrents before entering the finite-voltage regime, while narrower constrictions promote earlier suppression of the order parameter and the onset of current-induced dissipation. The device geometry also reshapes the spatial vortex distribution, indicating that weak-link design enables simultaneous control of transport characteristics and mixed-state behavior. Overall, our findings demonstrate that asymmetric superconducting loops incorporating non-equivalent constriction-type weak links provide a straightforward and efficient means of geometrically controlling vortex entry, phase-slip behavior, and critical currents in mesoscopic superconducting circuits. Such geometry-driven tunability could be valuable for engineering superconducting devices in which the local weak-link characteristics, the onset of finite voltage, and the vortex arrangement can be modified without altering the underlying superconducting material.

V. CONFLICT OF INTEREST

The authors declare no conflict of interest.

VI. AUTHOR CONTRIBUTIONS

All authors contributed equally to the entire manuscript.

VII. ETHICS, CONSENT TO PARTICIPATE, AND CONSENT TO PUBLISH DECLARATIONS

not applicable.

VIII. FUNDING DECLARATION

C. Aguirre thanks the CNPq grant number process: 174045/2023-9 for financial support. J. Fáundez acknowledges the support from ANID Fondecyt grant number 3240320. Powered@NLHPC: This research was partially supported by the NLHPC supercomputing infrastructure (CCSS210001).

IX. ACKNOWLEDGMENTS

C. Aguirre acknowledges S. Aguirre and M. Aguirre for useful discussions.

X. REFERENCES

[1] B. J. Baelus, K. Kadowaki, and F. M. Peeters, Influence of surface defects on vortex penetration and expulsion in mesoscopic superconductors, Phys. Rev. B **71**, 024514 (2005).

[2] G. J. Kimmel, A. Glatz, V. M. Vinokur, and I. A. Sadovskyy, Edge effect pinning in mesoscopic superconducting strips with non-uniform distribution of defects, Sci. Rep. **9**, 211 (2019).

[3] V. V. Moshchalkov, L. Gielen, C. Strunk, R. Jonckheere, X. Qiu, C. Van Haesendonck, and Y. Bruynseraede, Effect of sample topology on the critical fields of mesoscopic superconductors, Nature **373**, 319–322 (1995).

[4] P. G. de Gennes, *Superconductivity in Metals and Alloys* (Addison-Wesley, Reading, MA, 1989).

[5] L. R. Cadorim, A. R. de C. Romaguera, I. G. de Oliveira, R. R. Gomes, M. M. Doria, and E. Sardella, Intermediate type-I superconductors in the mesoscopic scale, Phys. Rev. B **103**, 014504 (2021).

[6] J. Clarke, SQUID fundamentals, in *SQUID Sensors: Fundamentals, Fabrication and Applications*, edited by H. Weinstock, NATO ASI Series E, Vol. 329 (Springer, Dordrecht, 1996). https://doi.org/10.1007/978-94-011-5674-5_1.

[7] J. R. Kirtley and J. P. Wikswo Jr., Scanning SQUID microscopy, Annu. Rev. Mater. Sci. **29**, 117–148 (1999).

[8] R. C. Jaklevic, J. Lambe, A. H. Silver, and J. E. Mercereau, Quantum interference effects in Josephson tunneling, Phys. Rev. Lett. **12**, 159–160 (1964).

[9] J. E. Zimmerman and A. H. Silver, Macroscopic quantum interference effects through superconducting point contacts, Phys. Rev. **141**, 367–375 (1966).

[10] M. Yu *et al.*, Sketched nanoscale $KTaO_3$-based superconducting quantum interference device, Phys. Rev. X **15**, 011037 (2025).

[11] S. Etaki, M. Poot, I. Mahboob, H. Yamaguchi, and H. S. J. van der Zant, Motion detection of a micromechanical resonator embedded in a d.c. SQUID, Nat. Phys. **4**, 785–788 (2008).

[12] S. Karan, H. Huang, C. Padurariu, *et al.*, Superconducting quantum interference at the atomic scale, Nat. Phys. **18**, 893–898 (2022).

[13] L. Nulens, H. Dausy, M. J. Wyszyński, B. Raes, M. J. Van Bael, M. V. Milošević, and J. Van de Vondel, Metastable states and hidden phase slips in nano-bridge SQUIDs, Phys. Rev. B **106**, 134518 (2022).

[14] D. Y. Vodolazov, F. M. Peeters, M. Morelle, and V. V. Moshchalkov, Masking effect of heat dissipation on the current-voltage characteristics of a mesoscopic superconducting sample with leads, Phys. Rev. B **71**, 184502 (2005).

[15] G. R. Berdiyorov, M. V. Milošević, L. Covaci, and F. M. Peeters, Rectification by an imprinted phase in a Josephson junction, Phys. Rev. Lett. **107**, 177008 (2011).

[16] W. Gillijns, A. V. Silhanek, V. V. Moshchalkov, and C. J. Olson Reichhardt, Origin of reversed vortex ratchet motion, Phys. Rev. Lett. **99**, 247002 (2007).

[17] W. D. Gropp, H. G. Kaper, G. K. Leaf, D. M. Levine, M. Palumbo, and V. M. Vinokur, Numerical simulation of vortex dynamics in type-II superconductors, J. Comput. Phys. **123**, 254–266 (1996).

[18] Ž. L. Jelić, M. V. Milošević, and A. V. Silhanek, Velocimetry of superconducting vortices based on stroboscopic resonances, Sci. Rep. **6**, 35687 (2016).

[19] J. E. González, O. A. González, and J. Barba-Ortega, Vortex and anti-vortex states in superconducting membrane with structural anomalies, Appl. Phys. A **132**, 79 (2026).

[20] E. Vega Ramirez, L. Becerra-Londoño, M. R. Joya, J. Barba-Ortega, and C. A. Aguirre, Vortex matter in superconducting films with different nanopatterns, Int. J. Mod. Phys. B **40**, 2650028 (2026).

[21] L. Bishop-Van Horn, py**TDGL**: Time-dependent Ginzburg–Landau in Python, Comput. Phys. Commun. **291**, 108799 (2023).

[22] M. Nadeem, M. S. Fuhrer, and X. Wang, The superconducting diode effect, Nat. Rev. Phys. **5**, 558–577 (2023).

[23] A. Daido, Y. Ikeda, and Y. Yanase, Intrinsic superconducting diode effect, Phys. Rev. Lett. **128**, 037001 (2022).

[24] S. Ilić and F. S. Bergeret, Theory of the supercurrent diode effect in Rashba superconductors with arbitrary disorder, Phys. Rev. Lett. **128**, 177001 (2022).

[25] J. J. He, Y. Tanaka, and N. Nagaosa, A phenomenological theory of superconductor diodes, New J. Phys. **24**, 053014 (2022).

[26] J. Jiang, M. V. Milošević, Y.-L. Wang, Z.-L. Xiao, F. M. Peeters, and Q.-H. Chen, Field-free superconducting diode in a magnetically nanostructured superconductor, Phys. Rev. Applied **18**, 034064 (2022).

[27] B. Zinkl, K. Hamamoto, and M. Sigrist, Symmetry conditions for the superconducting diode effect in chiral superconductors, Phys. Rev. Research **4**, 033167 (2022).

[28] F. Liu, Y. M. Itahashi, S. Aoki, Y. Dong, Z. Wang, N. Ogawa, T. Ideue, and Y. Iwasa, Superconducting diode effect under time-reversal symmetry, Sci. Adv. **10**, eado1502 (2024).

[29] S. Banerjee and M. S. Scheurer, Altermagnetic superconducting diode effect, Phys. Rev. B **110**, 024503 (2024).

[30] A. Gutfreund, H. Matsuki, V. Plastovets, A. Noah, L. Gorzawski, N. Fridman, G. Yang, A. Buzdin, O. Millo, J. W. A. Robinson, and Y. Anahory, Direct observation of a superconducting vortex diode, Nat. Commun. **14**, 1630 (2023).

[31] M. Castellani, O. Medeiros, A. Buzzi, A. Foster, M. Colangelo, and K. K. Berggren, A superconducting full-wave bridge rectifier, Nat. Electron. **8**, 417–425 (2025).

[32] T. Golod and V. M. Krasnov, Demonstration of a superconducting diode-with-memory, operational at zero magnetic field with switchable nonreciprocity, Nat. Commun. **13**, 3658 (2022).

[33] C. A. Aguirre, J. Barba-Ortega, A. S. de Arruda, and J. Faundez, Superconducting diode effect in a meso-wedge geometry with Abrikosov vortices, SciPost Phys. Core **9**, 006 (2026).